Covariance-Based MD Simulation Analysis Pinpoints Nanobody Attraction and Repulsion Sites on SARS-CoV-2 Omicron Spike Protein

Mert Golcuk[1], Fareeda E. Abu-Juam[1], Derman Basturk[2,3], Ayten Dilara Gursel[4], Clara Xazal Buran[4], Reyhan Metin Akkaya[4], Ahmet Yildiz[5,6], Mert Gur[1*]

[1] Department of Computational and Systems Biology, School of Medicine, University of Pittsburgh, Pittsburgh, PA, 15213, USA

[2] Department of Biology, Friedrich-Alexander-University Erlangen-Nürnberg, Erlangen 91058, Germany

[3] Max Planck Center for Physics and Medicine, Erlangen 91054, Germany

[4] Department of Mechanical Engineering, Istanbul Technical University (ITU), 34437, Istanbul, Turkey

[5] Physics Department, University of California, Berkeley, CA, USA

[6] Department of Molecular and Cell Biology, University of California, Berkeley, CA, USA

*Corresponding Author: Mert Gur, gurmert@pitt.edu

ABSTRACT

Omicron's heavily mutated SARS-CoV-2 spike receptor-binding domain (RBD) enables broad escape from neutralizing antibodies and nanobodies (Nbs), yet the atomistic basis of epitope-dependent Nb loss remains unclear. We performed >8 μs of all-atom molecular dynamics (MD) simulations of 13 Nbs (H11-D4, H11-H4, Huo-H3, MR17, NB21, NM1230, RE5D06, SB14, SB23, SB45, Ty1, VHH-E, WNB2) bound to the Omicron RBD to characterize binding-pose stability and interfacial dynamics. Principal-component analysis of MD trajectories yields binding-pose free-energy landscapes: most Nbs occupy single dominant basins yet often deviate from WTbound poses (orientation shifts), whereas NB21 and SB14 show pose plasticity. Using our covariance-matrix–based interaction-mapping method, we map stabilizing versus destabilizing residue–residue couplings and classify the underlying attractive interactions (salt bridges, hydrogen bonds, hydrophobic contacts) and repulsive interactions (like-charge repulsion or polarity mismatches). Attractive contacts converge on recurrent hydrophobic "anchor" patches on the receptor-binding motif (RBM) (~V445-G456 and ~F490-Y501) alongside binder-specific, complementarity-determining-region (CDR)-shaped interactions. Omicron substitutions rewire contact networks, shift binding orientations, and can introduce unfavorable repulsion, directly at mutation sites (e.g., E484A) or indirectly via mutation-driven reorientation, weakening binding. Mutation-induced repulsion reshapes correlated interfacial motions and reduces interfacial stability, providing a mechanistic basis for diminished binding robustness of multiple Nbs that were effective against WT and/or earlier variants. Low-speed steered MD pulling (AFM comparable) of ACE2 and selected Nbs shows lower unbinding work for Nbs than ACE2 (~16–42

vs ~45 kcal/mol), with NM1230 and SB23 most mechanically robust. These Nb–RBD interaction fingerprints pinpoint epitope-specific determinants and mutation-induced clash sites, providing a blueprint for structure-guided CDR engineering of Nbs with sustained potency against ongoing SARS-CoV-2 evolution.

INTRODUCTION

Nanobodies (Nbs) are single-domain antibody (Ab) fragments (~12–15 kDa) derived from camelid heavy-chain Abs that offer unique advantages as therapeutics and diagnostics.[1,2] Despite their small size, the three Nb complementarity-determining regions (CDR1–3) mediate specific and high affinity binding with target antigens (**Figure 1A**). Their compact, monomeric structure and often elongated CDR3 loop enables Nbs to bind cryptic epitopes on target proteins that are frequently inaccessible to conventional Abs.[3] In addition, Nbs exhibit high stability and affinity, comparable to full length Abs, which are on average an order of magnitude larger than Nbs, making them powerful neutralizing agents in viral infections. Nbs' compact size, increased stability and ability to bind cryptic epitopes make them well suited to engage and neutralize structurally complex, conformationally dynamic viral antigen assemblies, such as the trimeric, heavily glycosylated SARS-CoV-2 spike protein displayed on intact virions.

Since the emergence of SARS-CoV-2, various Nbs have been identified that target the spike (S) glycoprotein's receptor-binding domain (RBD), blocking its interaction with the human angiotensin converting enzyme-2 (ACE2) receptor.[4] For example, Nb H11-H4 can bind the RBD without overlapping ACE2 and effectively displace ACE2 via electrostatic repulsion, whereas Nb Ty1 binds the RBD at the ACE2 site (competing directly with the receptor).[4] Such mechanistic differences illustrate the diversity of how Nbs neutralize the virus, and they underscore the importance of mapping Nb–RBD interactions in detail.

However, SARS-CoV-2 has continued to evolve, accumulating a succession of mutations that enable emerging variants to evade existing Abs and prolong the pandemic. Consistent with ongoing antigenic drift, many monoclonal Abs (mAbs) and Nbs that were highly effective against the wild type (WT) strain have progressively lost potency with the emergence of the Delta and Omicron variants.[5] In fact, neutralizing effect of >85% of tested RBD-targeted Abs was diminished by Omicron mutations.[6] This reduced the clinical efficacy of several Ab therapies and led to the revocation of some emergency use therapeutic authorizations (EUAs). Collectively, these findings underscore that each emergent variant may necessitate new or re-engineered Abs/Nbs, and that rapid, systematic evaluation of Ab/Nb–antigen interactions, particularly how RBD mutations alter binding, is critical.

The Omicron lineage particularly carries a large number of mutations, many clustered in the spike RBD (**Figure 1B**).[7,8] This domain is crucial for viral infectivity by mediating ACE2 binding and viral entry, has therefore been a principal target for vaccines, mAbs, and Nbs.[9] Within the spike RBD, the ACE2-contacting receptor-binding motif (RBM; ~S438–Q506) is often described by three structural elements: the receptor-binding ridge (RBR; ~ T470–C488), the S443–N450 loop,

and an intervening relatively flat surface. Alternatively, the same RBD–ACE2 interface can be partitioned into three contact regions (CR1–CR3), with CR1 and CR3 at the two ends and CR2 forming the central β-strand region. (**Figure 1B**).[10] In this framework, CR1 overlaps with the ridge-dominated end of the RBM, CR2 corresponds to the central, more planar interface, and CR3 comprises the loop-containing end of the ACE2-contacting surface; notably, Omicron substitutions are distributed across all of these RBM and interface subregions.

Conventional experimental screening alone is not able keep pace with the rate of SARS-CoV-2 antigenic drift. In this context, all-atom molecular dynamics (MD) simulations have become a valuable tool for rapidly assessing how RBD mutations impact Ab/Nb binding at atomic resolution. MD simulations can capture the dynamic behavior of protein–protein interfaces and reveal changes in interaction networks and binding stability on nanosecond to microsecond timescales. Notably, our previous studies used MD simulations to elucidate the binding mechanisms of Nbs against earlier variants,[4] providing insight into how mutations in Alpha, Beta, and Delta variants alter Nb efficacy.

In this work, we perform extensive (>8 μs) physics-based all-atom MD simulations to characterize previously unresolved binding modes and interfacial dynamics of a panel of nanobodies (H11-D4,[11] H11-H4,[11] Huo-H3,[12] MR17,[13] NB21,[14] NM1230,[15] RE5D06,[16] SB14,[17] SB23,[18] SB45,[17] Ty1,[19] VHH-E,[20] and WNB2[21]) bound to the Omicron variant receptor-binding domain (RBD) of the SARS-CoV-2 spike glycoprotein. For each Nb, we identify the dominant bound conformations and apply our recently developed covariance-matrix–based method to extract key stabilizing and destabilizing residue–residue contacts that govern Nb–RBD recognition. The simulations further show that Omicron-specific substitutions can remodel these interfaces by altering binding orientation, modulating relative Nb–RBD motions, and rewiring hydrogen-bond, salt-bridge, and hydrophobic interaction networks. These atomic-level insights can serve as a blueprint for engineering next-generation Nbs with sustained potency against emerging SARS-CoV-2 variants.

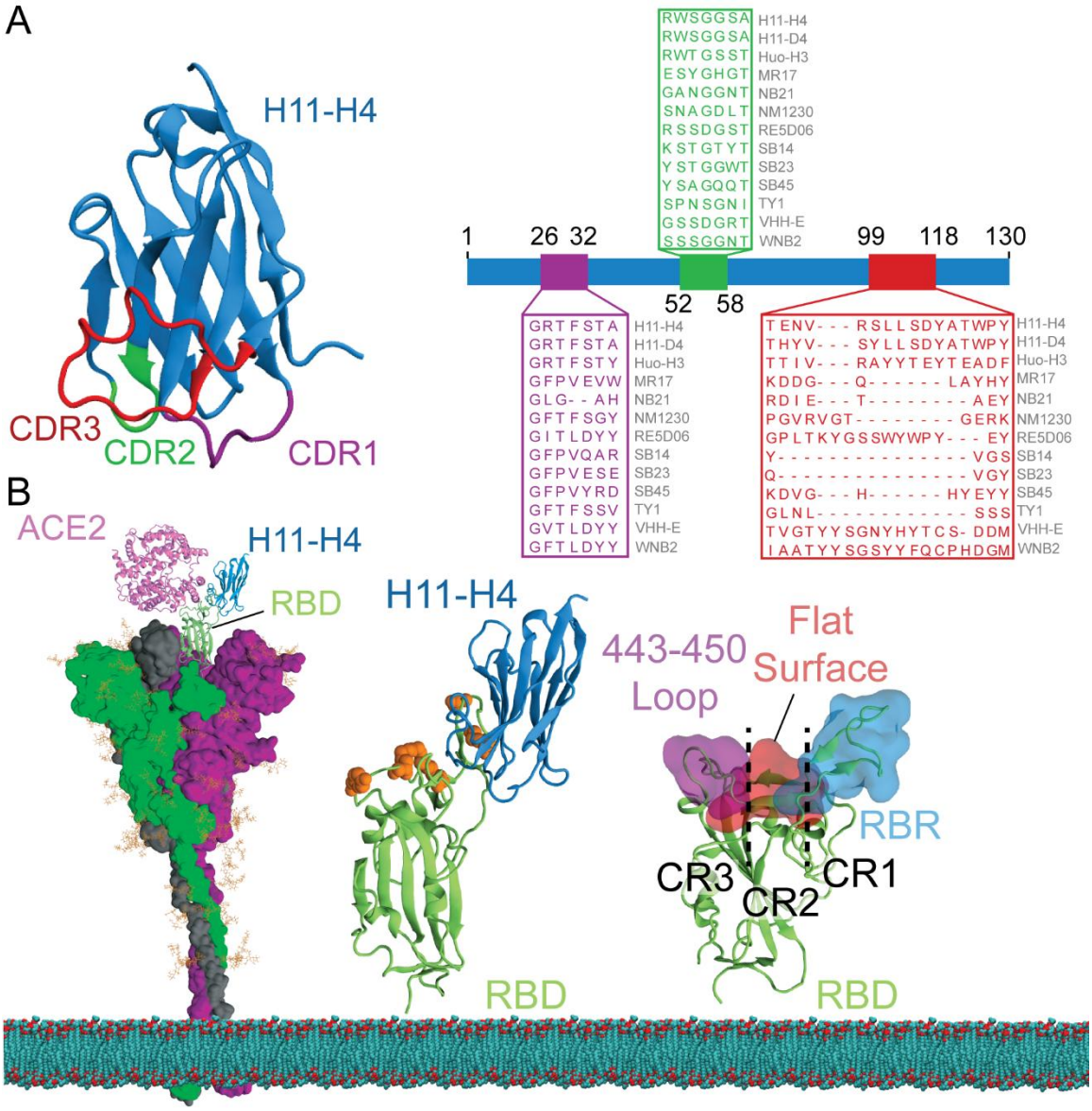

Figure 1. **Nanobody CDR architecture and overlap with the Omicron RBD–ACE2 interface.** *(A) Cartoon representation of the Nb variable domain (blue) with CDRs highlighted: CDR1 (residues G26–A32 for Nb H11-H4, magenta), CDR2 (residues R52–A58 for Nb H11-H4, green), and CDR3 (residues T99–Y118 for Nb H11-H4, red). Nb H11-H4 is shown as a reference example, and the right panel shows ClustalO*[22] *multiple sequence alignments (aligned by the entire nanobody sequence) of CDR1–3 from H11-H4 and other Nbs, illustrating the typically greater sequence diversity and length variability of CDR3*[23] *compared with CDR1 and CDR2. (B) Structural model of the Omicron SARS-CoV-2 spike trimer (surface) with the receptor-binding domain (RBD; green) bound by Nb (blue) and superposed with ACE2 (purple), showing that the Nb targets the ACE2-binding surface. The lipid bilayer is shown at the bottom. Center, closeup of the H11H4–RBD complex (RBD in green) with highlighted omicron mutation sites shown as orange spheres. Right, surface representation of the RBD highlighting the RBR (blue), the 443–*

450 loop (purple), and an adjacent flat surface (salmon), with regions labeled CR1–CR3 indicated. Omicron substitutions (T478K, E484A, Q493R, Q498R, N501Y) are shown as orange spheres.

METHODOLOGY

MD Simulations of Nanobody–Omicron RBD Complexes

We performed extensive all-atom MD simulations for each Nb–RBD complex to characterize binding dynamics. Simulations were performed on the SARS-CoV-2 Omicron BA.5 S glycoprotein's RBD, which includes the array of mutations characteristic of this variant. Initial atomic coordinates for the RBD-Nb complexes were obtained by homology modeling based on known SARS-CoV-2 RBD-Nanobody complexes (Table 1). N-linked glycosylation at N343 on the RBD was included based on our previous studies. Each complex was placed in a cubic simulation box with a 25 Å padding of TIP3P explicit water model in all directions, ensuring ~50 Å separation between periodic images. The solvated system was neutralized, and ion concentration was set to 0.15 M NaCl. The final systems' sizes ranged from 135,000 to 170,000 atoms (Table 1).

The omicron RBD-Nb complexes were energy minimized for 10,000 steps to relieve steric clashes, followed by a multi-stage equilibration protocol. Initially, protein heavy atoms were restrained, and water and ion molecules were relaxed for 2 ns, then a second 10,000 steps of minimization was performed without any restraints. Further equilibration ensued for ~4 ns with harmonic restraints on C_α atoms, followed by an additional unrestrained equilibration of ~4 ns that allowed the complexes to fully adapt to the simulation conditions. Production MD simulations were run in the NPT ensemble using NAMD 3[24] with the CHARMM36[25] force field. Temperature was maintained at 310 K with a Langevin thermostat and pressure at 1 atm with a Langevin barostat, using a 2 fs time step. Long-range electrostatics were computed with the Particle Mesh Ewald (PME) method and a real-space cutoff of 12 Å for van der Waals interactions. Periodic boundary conditions were applied in all dimensions. Each RBD–Nb system was simulated in two independent MD trajectories; each trajectory was 400 ns in length, yielding a total of 800 ns of simulation time per RBD–Nb type and 8.8 μs across all complexes. Coordinates were recorded every 50 ps.

Table 1. SARS-CoV-2 RBD-Nanobody Complexes and system sizes.

Nanobody	PDB ID	System Size (atoms)
H11-D4	6YZ5[11]	~150,000
H11-H4	6ZBP[11]	~150,000
Huo-H3	7OAQ[12]	~135,000
MR17	7C8W[13]	~160,000
NB21	7MDW[14]	~150,000
NM1230	7B27[15]	~140,000
RE5D06	7OLZ[16]	~170,000
SB14	7MFU[17]	~140,000
SB23	7A29[18]	~135,000
SB45	7N0G[17]	~140,000
Ty1	6ZXN[19]	~145,000
VHH-E	7KN5[20]	~160,000
WNB2	7LX5[21]	~155,000

Steered MD Simulations

All SMD simulations were performed with a constant pulling velocity of 0.1 Å ns^{-1}, a velocity chosen to approximate quasi-equilibrium unbinding and to remain comparable to high-speed atomic force microscopy (AFM) experiments. A harmonic potential was implemented by attaching a virtual spring (spring constant 100 kcal mol^{-1} $Å^{-2}$) between a dummy atom and the center of mass of the steered atoms.

The steered atoms consisted of the C_α atoms of all nanobody residues, while the fixed group comprised the C_α atoms of RBD residues forming the complementary interfacial region between Nb-RBD. The pulling direction was defined as the vector connecting the center of mass of the fixed atoms to that of the steered atoms at the start of each simulation.

Each SMD simulation was performed for 300 ns, corresponding to a total pulling distance of approximately 30 Å, which was sufficient to achieve complete detachment of the nanobody from the RBD in all simulations. The instantaneous force applied to the steered atoms was recorded throughout the trajectory, and the mechanical work associated with nanobody unbinding was calculated by integrating the force along the reaction coordinate.

Construction of binding-pose free-energy surfaces by PCA and generation of basin-specific conformational ensembles

Principal component analysis (PCA)[26,27] was then performed on the Nb C_α coordinates to quantify dominant variations in the Nb binding pose relative to the RBD. Using the aligned Nb coordinates, we constructed the covariance matrix.[28]

$$\mathbf{K} = \langle (\mathbf{R}^{Nb} - \langle \mathbf{R}^{Nb} \rangle)(\mathbf{R}^{Nb} - \langle \mathbf{R}^{Nb} \rangle)^{\mathrm{T}} \rangle$$

where $\mathbf{R}^{\boldsymbol{Nb}}$ is the 3 N-dimensional configurational vector composed of the instantaneous Nb C_α coordinates (N is the number of Nb residues) and $\langle \mathbf{R}^{\boldsymbol{Nb}} \rangle$ denotes the trajectory average. Eigenvalue decomposition of **K** yields principal components (PCs) $\mathbf{p}_i$ and their variances σ_i:

$$\mathbf{K} = \sum_{i=1}^{3N} \sigma_i \mathbf{p}_i \, \mathbf{p}_{\boldsymbol{i}}{}^T$$

Each frame was projected onto the PCs as $\mathbf{r}_{\boldsymbol{i}} = \mathbf{p}_{\boldsymbol{i}}{}^T (\mathbf{R} - \langle \mathbf{R} \rangle)$. We focused on PC1 and PC2, which capture the dominant Nb reorientation/translation relative to the aligned RBD (the sign of a PC axis is arbitrary). The joint probability density $f(\mathbf{r_1}, \mathbf{r}_2)$ was converted to a two-dimensional potential of mean force (free-energy surface) using, $A(\mathbf{r_1}, \mathbf{r}_2) = -kTln\,(f(\mathbf{r_1}, \mathbf{r}_2)) + constant$.[29] Low-free-energy basins were defined by local minima in $A(\mathbf{r_1}, \mathbf{r_2})$ and the barriers separating them. Basin assignments were validated by monitoring CDR–RBD distances (**Figure S1**) to ensure that each basin corresponds to a distinct binding pose. MD simulation conformations within each basin boundary were extracted to generate basin-specific sub-trajectories, which were subsequently used as binding-state conformational ensembles for the residue–residue interaction mapping described below.

Covariance-Based Interaction Mapping

We applied our covariance-matrix–based method[30,31] to systematically map stabilizing (attractive) and destabilizing (repulsive) residue–residue interaction hotspots at the Nb–RBD interface from the MD simulations. The analysis proceeded in four steps:

(i) Interprotein normalized covariance (cross-correlation matrix) calculation: For each Nb–RBD complex, we computed the normalized covariance between the positional fluctuations of all Nb C_α atoms and all RBD C_α atoms. This yielded an $N_{Nb} \times N_{RBD}$ matrix (where N_{Nb} ~120 residues in the Nb, N_{RBD} 195 residues in RBD), in which each element *C(i,j)* quantifies the correlation of motions between Nb residue *i* and RBD residue *j*

$$\mathbf{C}(i,j) = \langle \Delta\mathbf{R}_i^{Nb} \cdot \Delta\mathbf{R}_j^{RBD} \rangle / \left[\langle (\Delta\mathbf{R}_i^{Nb})^{\mathbf{2}} \rangle \cdot \langle (\Delta\mathbf{R}_j^{RBD})^2 \rangle \right]^{1/2}$$

Here, $\Delta\mathbf{R}_i^{Nb}$ and $\Delta\mathbf{R}_j^{RBD}$ denote the displacement vectors of residues i and j (C_α atoms) from their time-averaged positions (after alignment), and $\langle \cdot \rangle$ denotes a time average over the trajectory. Positive $\mathbf{C}(i,j)$ indicates correlated motion, whereas negative $\mathbf{C}(i,j)$ indicates anticorrelated motion. For residue pairs that remain spatially proximal at the interface, strong positive or negative correlations can serve as signatures of persistent attractive contacts or dynamically coupled repulsive interactions, respectively. Residue pairs with large $|\mathbf{C}(i,j)|$ values are prioritized as candidate hotspots.

(ii) Spatial filtering to generate the close-contact covariance matrix: Because correlations can also arise from indirect/long-range coupling, we filtered candidate residue pairs by proximity. We retained only Nb–RBD residue pairs whose mean C_α-C_α distance over the simulation was ≤11 Å for positively correlated pairs and ≤13 Å for negatively correlated pairs; all other pairs were discarded, yielding a close-contact covariance matrix.

(iii) Interaction Identification and Classification: For residue pairs retained in the close-contact covariance matrix, we annotated the underlying interaction type(s) using geometric criteria evaluated across MD conformations. Attractive interactions were classified as salt bridges (oppositely charged side-chain groups within ~6 Å),[32] hydrogen bonds (donor–acceptor distance ≤3.5 Å and donor–H–acceptor angle ≥150°),[33] and hydrophobic contacts (nonpolar side chains within ~8 Å).[34] Repulsive interactions were flagged as same-charge electrostatic repulsion (like-charged side-chain groups within ≤12 Å) and hydrophobic–charged polarity mismatch (an aliphatic side chain within ~12 Å of a charged group).

(iv) Mapping Interaction Frequencies: For each classified residue pair, we computed its occupancy (percentage of frames satisfying the corresponding geometric criterion), yielding an interaction-frequency map for each Nb–RBD complex.

All steps were implemented using custom MATLAB scripts; VMD[35] was used for trajectory processing and visualization.

Steered Molecular Dynamics simulations (*In silico* pulling)

To estimate and compare the binding strengths of ACE2 and Nbs to the Omicron RBD, we performed SMD simulations in which the bound partner (ACE2 or Nb) is mechanically detached from the RBD at a constant pulling speed ("*in silico* pulling"). In this approach, a dummy atom is moved with constant velocity along a predefined pulling direction, and the steered atoms are coupled to this dummy atom through a virtual spring. The instantaneous force and the accumulated mechanical work required for unbinding provide a quantitative measure of force-induced detachment and enable relative comparison among binders under identical simulation settings.

All SMD simulations were performed at a constant pulling velocity of 0.1 Å ns^{-1} with a spring constant of 100 kcal mol^{-1} $Å^{-2}$, consistent with a stiff-spring regime in which the center of mass of the steered group follows the dummy atom closely while still allowing thermal fluctuations. The guiding potential is defined as

$$\mathbf{F} = -\nabla U$$

$$U = \frac{k}{2}[(\mathbf{R}(t) - \mathbf{R}_0) \cdot \mathbf{n} - vt]^2$$

where U is the harmonic guiding potential, k is the spring constant, v is the pulling velocity, t is time, $\mathbf{n}$ is the unit vector defining the pulling direction, $\mathbf{R}(t)$ is the instantaneous center-of-mass position of the steered atoms, and $\mathbf{R}_0$is their initial center-of-mass position. The mechanical work

along the reaction coordinate ξ was computed by integrating the applied force along the pulling displacement,

$$W(\xi) = \int F(\xi)\, d\xi.$$

During the SMD simulations, C_α atoms were used for defining both steered and fixed atom groups. The steered atoms were defined as all C_α atoms of ACE2 for ACE2–RBD pulling, and all C_α atoms of the Nb for Nb–RBD pulling. The fixed atoms were defined as C_α atoms of three Omicron RBD segments (Y396–I402, C432–W436, and R509–F515), which served as an internal structural anchor for the RBD throughout pulling. The pulling direction **n** was defined as the vector from the center of mass of the fixed atoms (RBD anchor group) to the center of mass of the steered atoms (ACE2 or Nb) at the start of each simulation (**Figure 5B**).

Each SMD simulation was run for 300 ns, corresponding to an overall pulling distance of approximately 30 Å. Multiple independent SMD trajectories were performed for each ACE2–RBD or Nb–RBD complex, initiated from four distinct bound conformations sampled from the two equilibrium conventional MD trajectories of each Nb.

RESULTS AND DISCUSSION

For each Nb–RBD complex, the two independent trajectories were concatenated and frames were aligned on the RBD Cα atoms to remove global translation/rotation and focus on relative interface motion

Molecular Dynamics simulations reveal Omicron-dependent shifts in nanobody binding-pose free-energy landscapes

To probe how Omicron-associated mutations in the SARS-CoV-2 spike RBD affect Nb binding poses, we performed all-atom MD simulations for 13 Nb–RBD complexes, corresponding to the following Nbs: H11-D4, H11-H4, Huo-H3, MR17, NB21, NM1230, RE5D06, SB14, SB23, SB45, Ty1, VHH-E, and WNB2. MD simulations can provide atomistic insight (within the limits of force-field accuracy and finite sampling) into how mutations perturb local environments and interfacial contacts, and how these changes modulate binding-pose stability and dynamics. Starting from experimentally resolved Nb–RBD binding poses, we introduced the Omicron substitutions *in silico* and carried out two independent 400 ns simulations for each complex (800 ns per Nb). Trajectory frames were aligned by least-squares fitting of the RBD C_α atoms to the WT RBD reference structure, allowing us to focus on Nb reorientation relative to the spike. We then quantified these pose changes using PCA of the Nb C_α coordinates from the aligned trajectories and projected all sampled conformations onto the first two principal components (PC1 and PC2). The resulting conformational densities were converted to two-dimensional free-energy landscapes (**Figure 2**). Across the Nb panel, 11 Nbs (H11-D4, H11-H4, Huo-H3, MR17, NM1230, RE5D06, SB23, SB45,

Ty1, VHH-E, and WNB2) remain largely confined to a single dominant low free energy basin (S1), with four of them (H11-D4, MR17, SB23, and SB45) showing two binding substates that exhibit slightly different Nb orientations (**Figure S2**) while preserving a similar CDR–RBD interfacial distance (**Figure S1**) . Although these 11 Nbs sample single binding states with omicron RBD, the extent of their pose agreement with the WT-bound reference pose varies substantially (**Figure 2** and **Figure S2**). For H11-H4, NM1230, MR17, SB45, and WNB2, the WT Spike pose projects within the dominant Omicron basin, whereas VHH-E and Ty1 places the WT pose on a peripheral region relative to the S1 minimum. In contrast, Huo-H3, RE5D06, and SB23 project the WT reference outside the populated Omicron basin. By comparison, NB21 and SB14 populate three well separated basins (S1–S3) (**Figure S2**), revealing pronounced pose plasticity under Omicron. In these multibasin cases, the WT pose aligns with the first populated Omicron binding state (S1) in the simulations. However, the additional well-separated basins correspond to lower-occupancy binding modes (visited for a small fraction of the combined 2×400 ns sampling), suggesting reduced stability of a single binding pose under Omicron and potentially resulting in decreased Omicron RBD binding affinity for these Nbs. In accord with these PCA-derived landscapes (i.e., the position of the projected WT pose relative to the S1 basin), the mean C_α RMSD of Omicron-sampled Nb poses relative to the WT-bound pose ranges from 2.5–8.2 Å for single pose-preserving Nbs, whereas it is substantially larger (and more variable) for the pose-plastic binders SB14 (20.36 ± 7.10 Å) and NB21 (27.99 ± 15.69 Å) (**Table S1**).

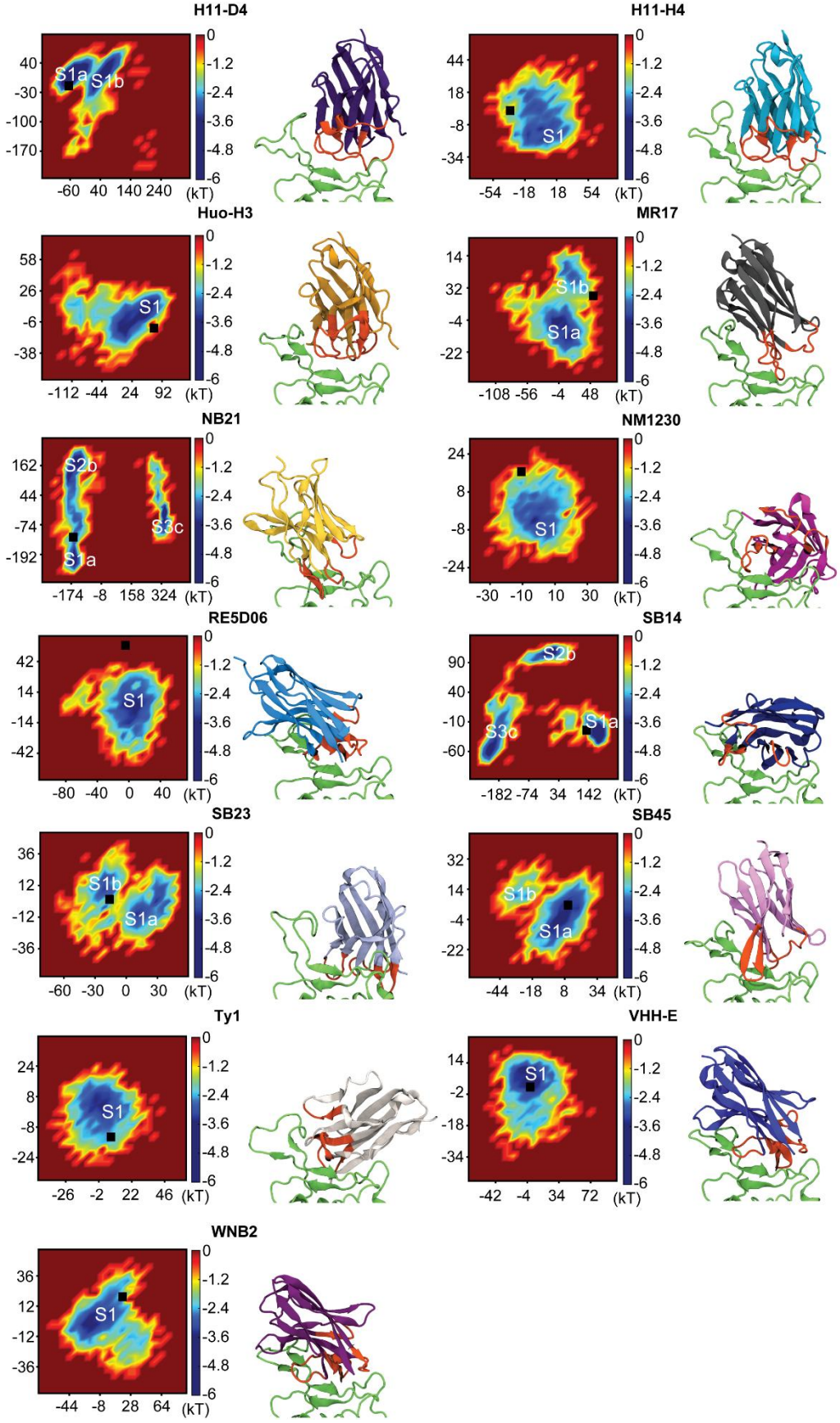
H11-D4
S1a
S1b
40
-30
-100
-170
-60 40 140 240
(kT)
H11-H4
S1
44
18
-8
-34
-54 -18 18 54
(kT)
Huo-H3
S1
58
26
-6
-38
-112 -44 24 92
(kT)
MR17
S1b
S1a
14
32
-4
-22
-108 -56 -4 48
(kT)
NB21
S2b
S3c
S1a
162
44
-74
-192
-174 -8 158 324
(kT)
NM1230
S1
24
8
-8
-24
-30 -10 10 30
(kT)
RE5D06
S1
42
14
-14
-42
-80 -40 0 40
(kT)
SB14
S2b
S3c
S1a
90
40
-10
-60
-182 -74 34 142
(kT)
SB23
S1b
S1a
36
12
-12
-36
-60 -30 0 30
(kT)
SB45
S1b
S1a
32
14
-4
-22
-44 -18 8 34
(kT)
Ty1
S1
24
8
-8
-24
-26 -2 22 46
(kT)
VHH-E
S1
14
-2
-18
-34
-42 -4 34 72
(kT)
WNB2
S1
36
12
-12
-36
-44 -8 28 64
(kT)
0
-1.2
-2.4
-3.6
-4.8
-6

Figure 2. Nbs sample single or multiple binding poses on the Omicron SARS-CoV-2 receptor-binding domain (RBD). *Each panel is labeled with the Nb name. For each Nb–RBD complex, two-dimensional free-energy surfaces are shown in the space of the first two principal components (PC1 and PC2) describing binding-pose variability. Free energies are plotted in units of kT and shifted by an arbitrary additive constant; the color scale ranges from 0 (red) to −6 kT (dark blue), with more negative values indicating more highly populated states. Dominant low-free-energy basins are labeled S1–S3 and used to define the most populated binding-pose states. Black squares (when present) indicate the WT reference binding pose projected into the same PC1–PC2 space. The position of the WT marker relative to the dominant Omicron basin provides a qualitative measure of pose preservation in this reduced coordinate system: proximity to the basin center indicates strong preservation, placement near the basin boundary indicates partial adjustment, and separation from the populated basin region indicates substantial rearrangement. Representative conformations taken from the free-energy minimum (darkest blue region) of the S1 basin are shown to the right of each free-energy surface (RBD, green; Nb, shown in distinct colors; CDR loops, orange/red).*

Correlated and anticorrelated interfacial motions pinpoint stabilizing and destabilizing hotspots at the Nb–Omicron RBD interface

For complexes that sampled multiple binding poses (**Figure 2B**), we partitioned each trajectory into basin-specific conformational ensembles corresponding to states S1–S3; for single-basin systems, the full bound-state trajectory was used as the analysis ensemble. Interpreting multi-microsecond MD trajectories of Nb–RBD complexes poses a major data-reduction challenge, because exhaustive, frame-by-frame enumeration of all interfacial contacts quickly becomes impractical when hundreds of residue pairs contribute to binding. To enable a systematic and scalable comparison across the Nb panel examined here, we employed our recently developed covariance-matrix–based interaction-mapping method.[30,31] This approach constructs an interprotein normalized covariance (C_α–C_α cross-correlation) matrix from the aligned trajectories, applies a distance-based filter to focus on physically plausible contacts, and then identifies the attractive (stabilizing) and repulsive (destabilizing) interactions underlying these correlations using the geometric criteria described in Methods. By concentrating the analysis on the most informative regions of the interface, the workflow efficiently pinpoints the residue–residue interactions that stabilize or destabilize Nb binding. The resulting close-contact correlation matrices provide compact, dynamic fingerprints of each Nb–RBD interface (**Figure 3**).

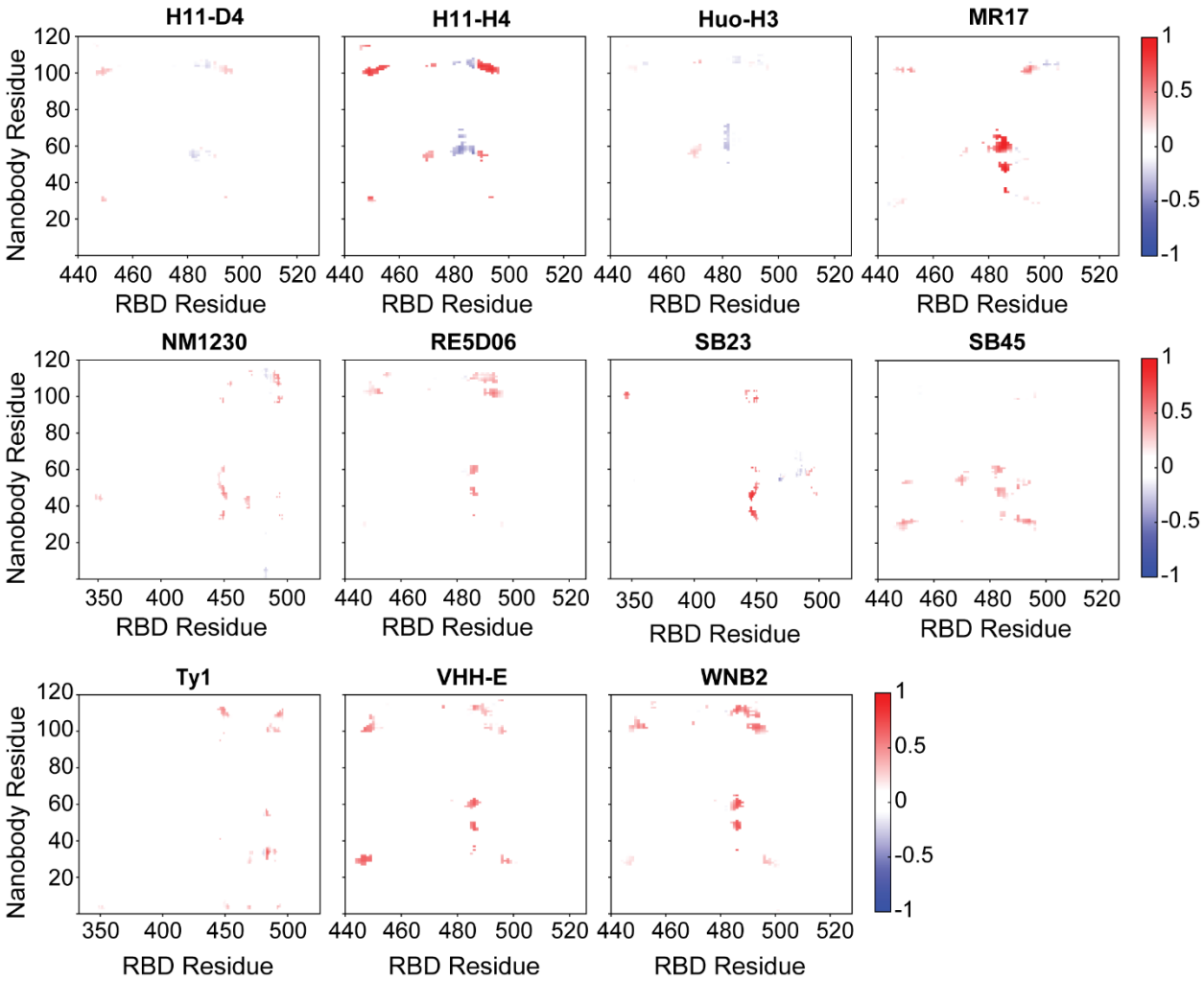

Figure 3. Interprotein C_α–C_α cross-correlation for nanobody–Omicron RBD complexes. Covariance for nanobody–Omicron RBD complexes. *Nbs H11-D4, H11-H4, Huo-H3, MR17, NM1230, RE5D06, SB23, SB45, Ty1, VHH-E, and WNB2. Each panel is a close-contact covariance matrix mapping residue–residue correlation between the Nb (y-axis, residue index) and the Omicron RBD (x-axis, residue index). In these two-dimensional maps, red regions correspond to residue pairs whose movements are positively correlated, indicating correlated interfacial motions ($\boldsymbol{C}(i,j)$ > 0), whereas blue regions highlight residue pairs that move in opposite directions and exhibit anticorrelated motions ($\boldsymbol{C}(i,j)$ < 0). Only residue pairs that come within contact range are shown (distant pairs filtered out), yielding close-contact covariance matrices that highlight dynamically coupled interfacial hotspots that were subsequently annotated as stabilizing or destabilizing based on interaction geometry).*

Covariance fingerprints classify Nb binding footprints across RBM sub-elements and the RBD core.

Close-contact covariance fingerprints (**Figure 3**) provide a compact "at-a-glance" summary of each Nb–RBD interface by reporting both (i) where the Nb couples to the RBD surface and (ii) whether those interfacial motions are dominated by correlated (stabilizing) or anticorrelated (potentially destabilizing) dynamics. Across the Nbs analyzed here, two coarse footprint classes emerge: most binders show RBM-focused coupling confined to the ACE2-contacting surface (~S438–Q506; e.g., H11-H4, Huo-H3, MR17, RE5D06, SB45, VHH-E, and WNB2), whereas a smaller subset retains RBM anchoring but additionally engages N-terminal/core residues (≈E340–R355; NM1230, SB23, and Ty1), consistent with broader binding footprints. Within the RBM-focused class, covariance hotspots further allow subdivision by RBM sub-element: S443–N450 loop–engaging binders (VHH-E and WNB2), a flat-surface–biased binder whose dominant contacts track the intervening planar RBM face (RE5D06), and ridge-weighted binders with substantial coupling across the receptor-binding ridge (RBR; ~T470–C488) (H11-H4, Huo-H3, MR17, and SB45). This qualitative separation is mirrored by the net covariance score (Scov; **Table S2**): interfaces with strongly positive totals (e.g., WNB2 and MR17) are dominated by correlated couplings, while Huo-H3 is the only case with near-zero/negative totals, reflecting substantial anticorrelated coupling and a higher burden of unfavorable contacts under Omicron.

Interaction-frequency mapping (**Figure 4**; **Table 2**; **Figure S3-4**) shows that, across binders, stabilizing contacts are overwhelmingly hydrophobic and converge on a recurrent RBM "anchor" centered near ~V445–F456 and ~F490–Y501, variably reinforced by hydrogen bonds or salt bridges and frequently involving Omicron-substituted sites (478, 484, 493, 498, and 501); T478K (WNB2, VHH-E), E484A (H11-H4, RE5D06, WNB2, Huo-H3, VHH-E, Ty1, SB45, NM1230, SB23), Q493R (MR17, Huo-H3, SB45, NM1230), Q498R (WNB2, SB23), N501Y (WNB2). Where Nbs differ most is in how much this shared RBM anchoring is offset by RBR-localized (and adjacent) repulsive contacts around ~Q474–A484 (often involving the E484A site): RE5D06, VHH-E, and Ty1 are essentially repulsion-free above the reporting threshold, whereas Huo-H3 (and, to lesser degrees, H11-H4, MR17, SB45, NM1230, and SB23) exhibits persistent polarity/charge mismatches that erode the net coupling. Overall, covariance fingerprints therefore connect epitope footprint (RBM-only vs core-spanning) to binding robustness (hydrophobic anchoring with minimal repulsion vs mutation-adjacent repulsion) in a single view; residue-level interaction partners, occupancies, and mutation-specific contacts for each Nb are provided in the "Detailed Interaction Information on Nb-Omicron RBD Interactions" section in the **supplementary materials**.

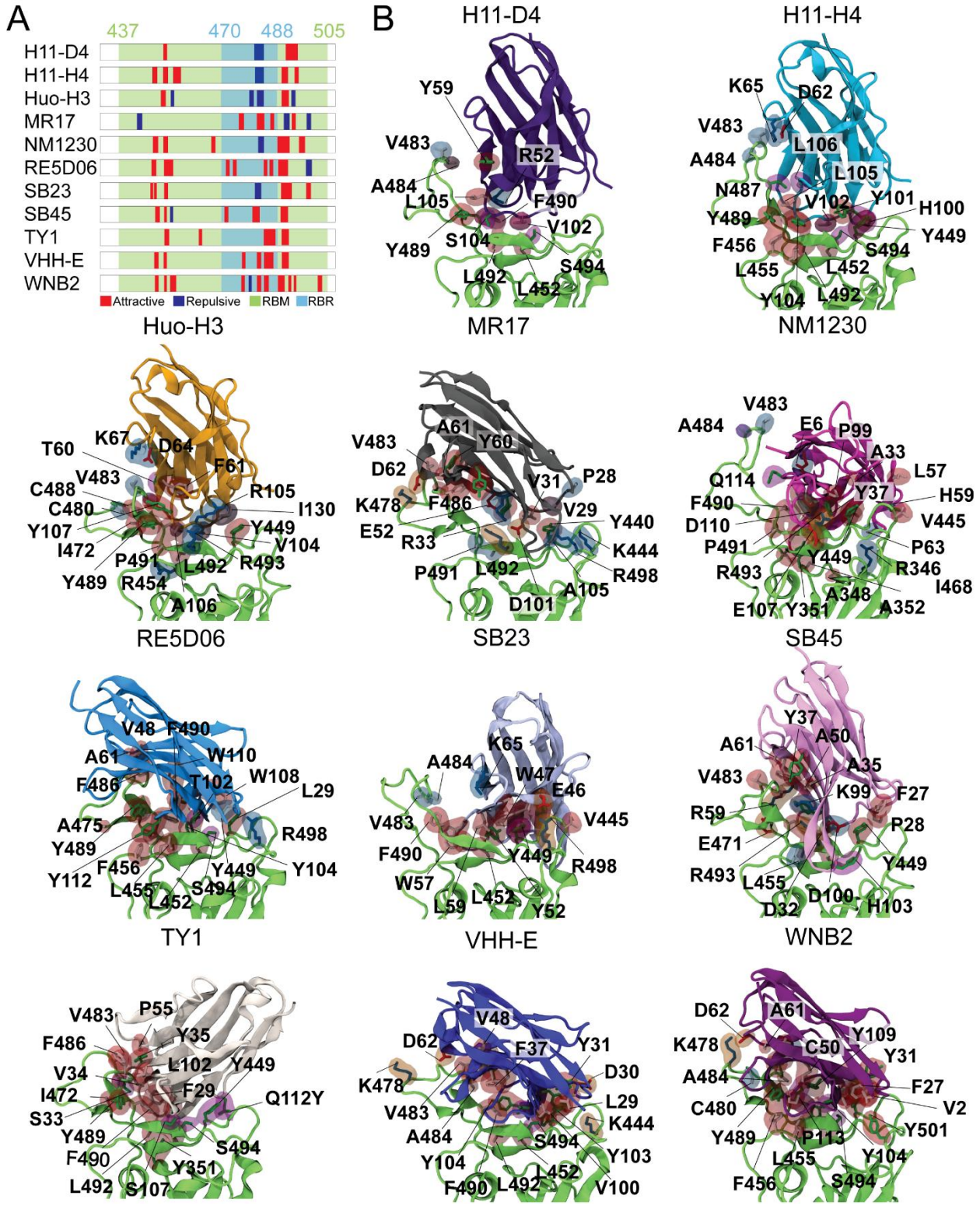

Figure 4. Structural mapping for nanobody–Omicron RBD interfaces at RBM. (A) *Linear map of residue-level interaction profiles for a panel of RBD-binding Nbs. The RBM sequence is highlighted from residue N437 to H505, encompassing the receptor-binding motif (RBM; green)*

and the RBD core outside the RBM (RBR; light blue). Colored bars indicate residues contributing attractive (red) or repulsive (blue) interactions between each Nb and the RBD. Nbs are listed on the left, and residue numbering along the top corresponds to the SARS-CoV-2 spike protein. This representation highlights shared and distinct interaction hotspots across Nbs. H11-D4, H11-H4, Huo-H3, MR17, NM1230, RE5D06, SB23, SB45, Ty1, VHH-E, and WNB2. Interactions of NM1230 involving residue R348 (repulsive), as well as A348, Y351, and A352, and the interaction of TY1 involving Y351, are not shown in the linear map. ***(B)*** *Structural visualization of the same interfaces, with each Nb bound to the Omicron RBD (green) and interacting RBD residues colored by interaction type: hydrophobic (red), salt bridge (orange), hydrogen bonding (magenta), and repulsive (blue). Only interactions with ≥14% occupancy over the full simulation are shown. H11-D4 (Dark Purple), H11-H4 (Cyan), Huo-H3 (Orange), MR17 (Gray), NM1230 (Magenta), RE5D06 (Blue), SB23 (Ice Blue), SB45 (Pink), Ty1 (White), VHH-E (Dark Blue), and WNB2 (Purple).*

Table 2. Interactions between Nbs and SARS-CoV-2 Omicron Variant. *Grouped interactions for the considered Nbs based on high-frequency (>%49) attractive interactions (Salt bridge, SB; Hydrogen bond, HB; Hydrophobic, HP) and medium-to-high (>%14) repulsive interactions (R; aliphatic-aliphatic, aliphatic polar).*

Nanobody	SB	HB	HP	R
H11-D4	0	0	4	2
H11-H4	0	2	8	4
Huo-H3	0	0	7	12
MR17	2	0	9	5
NM1230	2	0	12	3
RE5D06	0	0	14	1
SB23	0	1	11	2
SB45	2	0	12	2
TY1	0	1	15	0
VHH-E	1	0	13	0
WNB2	1	1	18	1

***In silico* pulling experiments show that nanobody binding affinities become substantially lower than ACE2 binging.**

To directly compare the mechanical stability of ACE2 binding and Nb binding to the Omicron RBD, and to rank binding strengths among the Nbs, we performed low-speed SMD pulling simulations (0.1 Å ns^{-1}; **Figure 5**). The resulting work profiles as a function of the reaction coordinate provide a consistent metric for comparing force-induced detachment under identical

pulling conditions and atom-group definitions. Furthermore, because by the second law of thermodynamics the mean non-equilibrium work satisfies $\langle W \rangle \geq \Delta G_{binding}$, the SMD unbinding work values provide an upper bound on the corresponding equilibrium free-energy change for unbinding. In these SMD simulations, ACE2 exhibits the highest resistance to detachment, with its work curve lying above the Nb curves throughout the pulling/reaction coordinate (**Figure 5A**), indicating that ACE2 forms the mechanically strongest complex with the Omicron RBD among the systems quantified here. The average work required to unbind ACE2 from the Omicron RBD is 45 kcal mol^{-1} (**Table 3**). In contrast, all Nbs required less work to detach from the Omicron RBD (16-42 kcal mol^{-1}), except for two Nbs, this reduction is substantial, requiring approximately 10-30 kcal mol^{-1} less work than ACE2. This indicates that, relative to ACE2, Omicron yields Nb–RBD interfaces that are mechanically easier to disrupt under force. In particular, Nbs H11-D4, H11-H4, and Ty1, which were previously shown[4] to exhibit work values comparable to (or slightly stronger than) ACE2 on the WT RBD, detach from the Omicron RBD with 15.54, 22.69, and 25.76 kcal mol^{-1}, respectively (**Table 3**), corresponding to just ~34.5%, ~50.4%, and ~57.2% of the ACE2 work value. Other Nbs quantified here also remain below ACE2, including Huo-H3 (23.84 kcal mol^{-1}), VHH-E (29.4 kcal mol^{-1}), and SB45 (31 kcal mol^{-1}), with H11-D4 (15.54 kcal mol^{-1}) being the weakest binder. Only two SB23 (41.81 kcal mol^{-1}), and NM1230 (42.46 kcal qmol^{-1}) retained relatively high work values, approaching ACE2 in mean work, though still not exceeding it (**Table 3**).

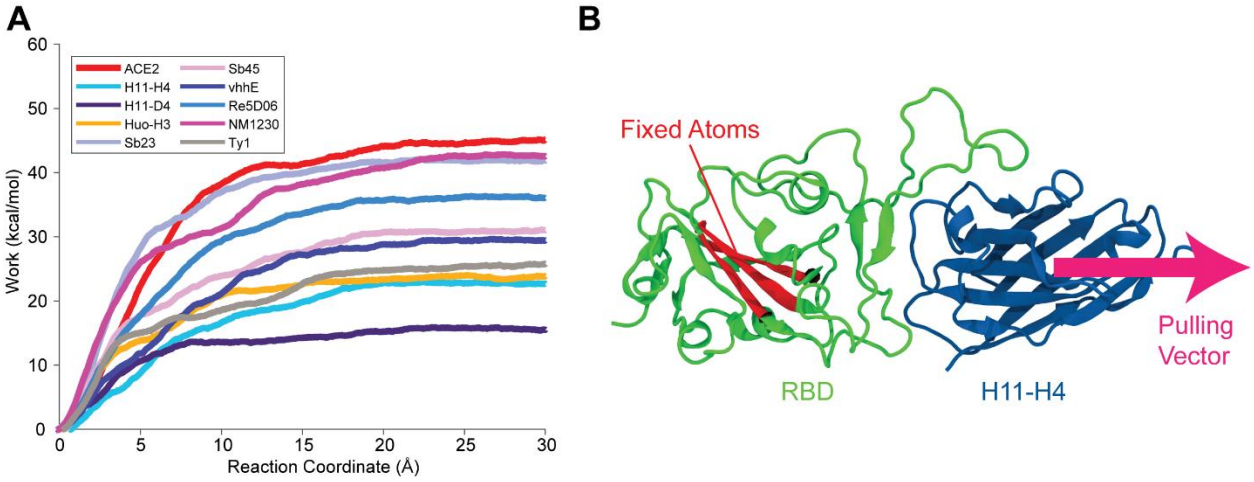

Figure 5. Force-induced detachment of ACE2 and nanobodies (Nbs) from the Omicron RBD. (A) *Average accumulated unbinding work, $W(\xi)$, as a function of the reaction coordinate ξ (center-of-mass displacement of the steered group along the pulling direction) obtained SMD simulations performed at a constant pulling velocity of 0.1 Å ns^{-1} (spring constant $k = 100$kcal mol^{-1} Å^{-2}). Curves are shown for ACE2 and for Nbs H11-H4, H11-D4, Huo-H3, SB23, SB45, VHH-E, RE5D06, NM1230, and Ty1. Final work values (mean ± s.d.) are summarized in Table 2.* ***(B)*** *Schematic of the SMD pulling setup (shown for the H11-H4–RBD complex as a representative example). The fixed atoms (red) are the RBD C_α atoms of residues Y396–I402, C432–W436, and R509–F515. The steered atoms consist of all C_α atoms of the bound partner (ACE2 or Nb), and*

the pulling direction (magenta arrow) is defined by the vector from the center of mass of the fixed group to the center of mass of the steered group at the start of each simulation.

Table 3. Work values of the ACE2 – RBD and the Nb – RBD systems. Systems that are listed as **NA**, indicate that a quantitative work value is not reported for those complexes in the present dataset.

System	Work (kcal/mol) ± std
ACE2 - RBD	44.99 ± 11.73
H11-D4 - RBD	15.54 ± 9.12
H11-H4 - RBD	22.69 ± 6.35
Huo-H3 - RBD	23.84 ± 7.22
MR17 – RBD	NA
NB21 – RBD	NA
NM1230 – RBD	42.46 ± 7.19
RE5D06 – RBD	36.01 ± 4.36
SB14 – RBD	NA
SB23 – RBD	41.81 ± 11.62
SB45 – RBD	31.00 ± 5.42
Ty1 – RBD	25.76 ± 8.14
VHH-E – RBD	29.40 ± 10.24
WNB2 – RBD	NA

CONCLUSION

In this study, we combined multi-microsecond all-atom MD simulations with a covariance-matrix–based interface mapping framework to dissect how Omicron (BA.5) RBD substitutions reshape Nb recognition at atomic resolution. By projecting MD trajectories onto PCA-derived binding-pose free-energy surfaces, we showed that most Nbs remain confined to a dominant bound basin on the Omicron RBD, but the degree of pose preservation varies widely across epitopes. Notably, a subset of binders exhibits pronounced pose plasticity (multiple basins and large deviations from the WT reference pose), consistent with confinement to a dominant binding pose and reduced interfacial stability under Omicron. These results emphasize that Omicron escape can arise not only from loss of individual contacts, but also from mutation-driven reorientation and increased heterogeneity of the bound ensemble.

Our covariance-based fingerprints and interaction-frequency maps then unify these pose-level changes with a residue-level mechanism. Across the Nb panel, stabilizing interactions are

dominated by hydrophobic contacts that repeatedly converge on an RBM "anchor" region centered near ~V445–G456 and ~F490–Y501, with binder-specific reinforcement from hydrogen bonds and salt bridges. Importantly, many of these recurrent contact networks are rewired by Omicron substitutions (e.g., around 478, 484, 493, 498, and 501), revealing how a shared geometric binding surface can nonetheless produce distinct energetic outcomes depending on CDR chemistry and local complementarity. Where Nbs differ most strongly is in their *repulsion burden*: several interfaces remain largely free of repulsive contacts above the reporting threshold, whereas others accumulate persistent polarity mismatches and/or like-charge repulsion, particularly near the ridge-adjacent region around ~Q474–A484 that includes the E484A site. Thus, Omicron-driven weakening is frequently explained by the introduction of unfavorable interactions and anticorrelated interfacial motions, rather than a simple disappearance of favorable contacts.

The force-induced detachment (SMD) simulations provide an independent, consistent ranking that ties these interaction-network trends to mechanical robustness. Under an identical pulling protocol, ACE2 requires the largest unbinding work, whereas the tested Nbs detach with substantially lower work values (approximately ~16–42 kcal/mol versus ~45 kcal/mol for ACE2). Within the Nb set, NM1230 and SB23 retain the highest resistance to detachment, while first-generation Nbs such as H11-H4, H11-D4, and Ty1 detach with markedly lower work, indicating that Omicron shifts the competitive binding landscape in favor of ACE2 under force. Although SMD work is not a direct equilibrium affinity ($\langle W \rangle \geq \Delta G_{binding}$), the work trends align with the covariance/interaction analyses: Nbs with extensive, persistent attractive networks and minimal repulsion exhibit greater mechanical stability, whereas mutation-adjacent repulsive features correlate with easier disruption of the interface.

Taken together, this work provides a coherent mechanistic picture of Omicron escape across diverse Nb epitopes: Omicron substitutions remodel binding by (i) shifting and broadening bound pose ensembles, (ii) preserving a small set of recurrent hydrophobic RBM anchors, and (iii) selectively introducing repulsive contacts and dynamically anticorrelated motions that erode net interfacial stability. More broadly, our covariance-based workflow converts long MD trajectories into compact, interpretable "interaction fingerprints" that pinpoint both *what to preserve* (shared anchor patches) and *what to fix* (mutation-induced clash/repulsion sites), offering actionable guidance for structure-guided CDR engineering toward broader variant robustness. By explicitly mapping where Omicron turns attraction into repulsion, this study lays a practical foundation for designing next-generation Nbs that remain effective as SARS-CoV-2 continues to evolve.

Funding

This work is supported by COVID-19 HPC Consortium (Grant number: TG-BIO210181).

REFERENCES

1 Bannas, P., Hambach, J. & Koch-Nolte, F. Nanobodies and Nanobody-Based Human Heavy Chain Antibodies As Antitumor Therapeutics. *Front Immunol* **8**, 1603 (2017). https://doi.org/10.3389/fimmu.2017.01603

2 Jin, B. K., Odongo, S., Radwanska, M. & Magez, S. NANOBODIES®: A Review of Diagnostic and Therapeutic Applications. *Int J Mol Sci* **24** (2023). https://doi.org/10.3390/ijms24065994

3 Zhu, H. & Ding, Y. Nanobodies: From Discovery to AI-Driven Design. *Biology (Basel)* **14** (2025). https://doi.org/10.3390/biology14050547

4 Golcuk, M., Hacisuleyman, A., Erman, B., Yildiz, A. & Gur, M. Binding Mechanism of Neutralizing Nanobodies Targeting SARS-CoV-2 Spike Glycoprotein. *J Chem Inf Model* **61**, 5152-5160 (2021). https://doi.org/10.1021/acs.jcim.1c00695

5 Liu, B. *et al.* Enhanced potency of an IgM-like nanobody targeting conserved epitope in SARS-CoV-2 spike N-terminal domain. *Signal Transduct Target Ther* **9**, 131 (2024). https://doi.org/10.1038/s41392-024-01847-8

6 Cao, Y. *et al.* Omicron escapes the majority of existing SARS-CoV-2 neutralizing antibodies. *Nature* **602**, 657-663 (2022). https://doi.org/10.1038/s41586-021-04385-3

7 Golcuk, M., Yildiz, A. & Gur, M. Omicron BA.1 and BA.2 variants increase the interactions of SARS-CoV-2 spike glycoprotein with ACE2. *Journal of Molecular Graphics and Modelling* **117**, 108286 (2022). https://doi.org/https://doi.org/10.1016/j.jmgm.2022.108286

8 Viana, R. *et al.* Rapid epidemic expansion of the SARS-CoV-2 Omicron variant in southern Africa. *Nature* **603**, 679-686 (2022). https://doi.org/10.1038/s41586-022-04411-y

9 Schoof, M. *et al.* An ultrapotent synthetic nanobody neutralizes SARS-CoV-2 by stabilizing inactive Spike. *Science* **370**, 1473-1479 (2020). https://doi.org/10.1126/science.abe3255

10 Taka, E. *et al.* Critical Interactions Between the SARS-CoV-2 Spike Glycoprotein and the Human ACE2 Receptor. *The Journal of Physical Chemistry B* **125**, 5537-5548 (2021). https://doi.org/10.1021/acs.jpcb.1c02048

11 Huo, J. *et al.* Neutralizing nanobodies bind SARS-CoV-2 spike RBD and block interaction with ACE2. *Nature Structural & Molecular Biology* **27**, 846-854 (2020). https://doi.org/10.1038/s41594-020-0469-6

12 Huo, J. *et al.* A potent SARS-CoV-2 neutralising nanobody shows therapeutic efficacy in the Syrian golden hamster model of COVID-19. *Nature Communications* **12**, 5469 (2021). https://doi.org/10.1038/s41467-021-25480-z

13 Li, T. *et al.* A synthetic nanobody targeting RBD protects hamsters from SARS-CoV-2 infection. *Nature Communications* **12**, 4635 (2021). https://doi.org/10.1038/s41467-021-24905-z

14 Sun, D. *et al.* Potent neutralizing nanobodies resist convergent circulating variants of SARS-CoV-2 by targeting diverse and conserved epitopes. *Nature Communications* **12**, 4676 (2021). https://doi.org/10.1038/s41467-021-24963-3

15 Wagner, T. R. *et al*. NeutrobodyPlex—monitoring SARS-CoV-2 neutralizing immune responses using nanobodies. *The EMBO Reports* **22**, EMBR202052325 (2021). https://doi.org/10.15252/embr.202052325

16 Güttler, T. *et al*. Neutralization of SARS-CoV-2 by highly potent, hyperthermostable, and mutation-tolerant nanobodies. *The EMBO Journal* **40**, EMBJ2021107985 (2021). https://doi.org/10.15252/embj.2021107985

17 Ahmad, J. *et al*. Structures of synthetic nanobody–SARS-CoV-2 receptor-binding domain complexes reveal distinct sites of interaction. *Journal of Biological Chemistry* **297** (2021). https://doi.org/10.1016/j.jbc.2021.101202

18 Custódio, T. F. *et al*. Selection, biophysical and structural analysis of synthetic nanobodies that effectively neutralize SARS-CoV-2. *Nature Communications* **11**, 5588 (2020). https://doi.org/10.1038/s41467-020-19204-y

19 Hanke, L. *et al*. An alpaca nanobody neutralizes SARS-CoV-2 by blocking receptor interaction. *Nature Communications* **11**, 4420 (2020). https://doi.org/10.1038/s41467-020-18174-5

20 Koenig, P.-A. *et al*. Structure-guided multivalent nanobodies block SARS-CoV-2 infection and suppress mutational escape. *Science* **371**, eabe6230 (2021). https://doi.org/doi:10.1126/science.abe6230

21 Pymm, P. *et al*. Nanobody cocktails potently neutralize SARS-CoV-2 D614G N501Y variant and protect mice. *Proceedings of the National Academy of Sciences* **118**, e2101918118 (2021). https://doi.org/doi:10.1073/pnas.2101918118

22 Sievers, F. *et al*. Fast, scalable generation of high-quality protein multiple sequence alignments using Clustal Omega. *Mol Syst Biol* **7**, 539 (2011). https://doi.org/10.1038/msb.2011.75

23 Xiang, Y. *et al*. Integrative proteomics identifies thousands of distinct, multi-epitope, and high-affinity nanobodies. *Cell Systems* **12**, 220-234.e229 (2021). https://doi.org/10.1016/j.cels.2021.01.003

24 Phillips, J. C. *et al*. Scalable molecular dynamics on CPU and GPU architectures with NAMD. *The Journal of Chemical Physics* **153** (2020). https://doi.org/10.1063/5.0014475

25 Huang, J. & MacKerell Jr, A. D. CHARMM36 all-atom additive protein force field: Validation based on comparison to NMR data. *Journal of Computational Chemistry* **34**, 2135-2145 (2013). https://doi.org/https://doi.org/10.1002/jcc.23354

26 Yang, L. W., Eyal, E., Bahar, I. & Kitao, A. Principal component analysis of native ensembles of biomolecular structures (PCA_NEST): insights into functional dynamics. *Bioinformatics* **25**, 606-614 (2009). https://doi.org/10.1093/bioinformatics/btp023

27 Amadei, A., Linssen, A. B. & Berendsen, H. J. Essential dynamics of proteins. *Proteins* **17**, 412-425 (1993). https://doi.org/10.1002/prot.340170408

28 Ichiye, T. & Karplus, M. Collective motions in proteins: a covariance analysis of atomic fluctuations in molecular dynamics and normal mode simulations. *Proteins* **11**, 205-217 (1991). https://doi.org/10.1002/prot.340110305

29 Gur, M., Zomot, E. & Bahar, I. Global motions exhibited by proteins in micro-to milliseconds simulations concur with anisotropic network model predictions. *The Journal of chemical physics* **139**, 09B612_611 (2013).

30 Gur, M. & Erman, B. Quasi-harmonic fluctuations of two bound peptides. *Proteins* **80**, 2769-2779 (2012). https://doi.org/10.1002/prot.24160

31 Golcuk, M. & Gur, M. A Practical Covariance-Based Method for Efficient Detection of Protein–Protein Attractive and Repulsive Interactions in Molecular Dynamics Simulations. *Journal of Chemical Information and Modeling* **65**, 9865-9870 (2025). https://doi.org/10.1021/acs.jcim.5c01725

32 Beckstein, O., Denning, E. J., Perilla, J. R. & Woolf, T. B. Zipping and unzipping of adenylate kinase: atomistic insights into the ensemble of open<-->closed transitions. *J Mol Biol* **394**, 160-176 (2009). https://doi.org/10.1016/j.jmb.2009.09.009

33 Durrant, J. D. & McCammon, J. A. HBonanza: a computer algorithm for molecular-dynamics-trajectory hydrogen-bond analysis. *J Mol Graph Model* **31**, 5-9 (2011). https://doi.org/10.1016/j.jmgm.2011.07.008

34 Stock, P., Utzig, T. & Valtiner, M. Direct and quantitative AFM measurements of the concentration and temperature dependence of the hydrophobic force law at nanoscopic contacts. *J Colloid Interface Sci* **446**, 244-251 (2015). https://doi.org/10.1016/j.jcis.2015.01.032

35 Humphrey, W., Dalke, A. & Schulten, K. VMD: Visual molecular dynamics. *Journal of Molecular Graphics* **14**, 33-38 (1996). https://doi.org/https://doi.org/10.1016/0263-7855(96)00018-5